Journal of Materials Chemistry A

ROYAL SOCIETY OF CHEMISTRY

PAPER

View Article Online
View Journal | View Issue

Cite this: J. Mater. Chem. A, 2025, 13, 8024

Chemically bonded interface modulated S-scheme charge transfer in Sb_2S_3@$ZnIn_2S_4$ core–shell heterostructures for boosted catalytic activity toward nitrogen photofixation†

Cheng-Jie Zheng,[a] Chen Zhang,[a] Hao-Xiang Yang,[a] Tingting Chen,[a] Zhi-Cai He,*[a] Jian Zhang,[b] Guo-Bo Huang,*[a] Mingyuan Wang,*[c] Guiwu Liu[d] and Wei Chen*[a]

The exploration of efficient strategies for nitrogen photofixation driven by visible light at room temperature and atmospheric pressure is still highly desirable but remains a great challenge. In this study, hierarchical Sb_2S_3@$ZnIn_2S_4$ core–shell samples were synthesized through a hydrothermal reaction, in which ultrathin $ZnIn_2S_4$ nanosheets were tightly and uniformly wrapped on the surface of Sb_2S_3 nanorods. Systematic characterization revealed that the chemically bonded interface in Sb_2S_3@$ZnIn_2S_4$ core–shell heterostructures was critical to rapid charge separation, leading to a significant enhancement of photocatalytic performance for nitrogen photofixation. The optimal nitrogen photofixation system, namely, Sb_2S_3@$ZnIn_2S_4$-75, exhibited excellent performance achieving an ammonia concentration of 15.96 ± 0.97 mg L^{-1} after visible light irradiation for 40 min, which was approximately 1.88 and 7.19 times higher than those of relevant $ZnIn_2S_4$ and Sb_2S_3, respectively. Moreover, an S-scheme charge transfer route on Sb_2S_3@$ZnIn_2S_4$ core–shell heterostructures was proposed based on band structure analysis, *in situ* irradiated X-ray photoelectron spectroscopy (ISI-XPS) investigation, noble metal deposition, and density functional theory (DFT) simulation. This work gave a useful insight into the development of efficient photocatalysts for boosted photocatalytic activity toward nitrogen photofixation.

Received 12th December 2024
Accepted 6th February 2025

DOI: 10.1039/d4ta08841g

rsc.li/materials-a

Introduction

Ammonia (NH_3), as the basic raw material, is an indispensable fertilizer in agriculture, which is widely used in the manufacture of all nitrogen and nitrogen-containing fertilizers.[1] Besides, due to its high combustion calorific value, ammonia can also be used as an energy source by direct combustion or hydrogen production through its decomposition. Traditional ammonia synthesis has been accomplished at high temperature (300–500 °C) and extreme pressure (200–300 atm) in the presence of iron-based catalysts, namely the Haber–Bosch process, which consumes 1–2% of the world's energy supply and simultaneously produces more than 300 million tons of carbon dioxide annually.[2–4] In contrast, nitrogen photofixation to ammonia by light irradiation proceeds under ambient conditions without fossil fuel consumption and carbon dioxide emission, which represents a sustainable ammonia synthesis route. However, the catalytic efficiency for ammonia production through the photofixation strategy still cannot meet the requirements of industrial demand.[5] Therefore, it is urgently desired to design and construct efficient photo-driven catalysts with excellent catalytic activity and stability toward nitrogen photofixation.

Antimony sulfide (Sb_2S_3) is a typical binary transition metal sulfide with strong visible-light harvesting capacity due to its high absorption coefficient and narrow band gap,[6] which has been widely employed in various photocatalytic fields, such as hydrogen evolution from water splitting,[7,8] organic pollutant photodegradation,[9,10] and heavy metal reduction in aqueous solution.[11] But the disordered migration in pure Sb_2S_3 greatly accelerates the recombination kinetics of photogenerated charges, leading to low-efficient catalytic activity.[12] For effectively modifying the photocatalytic performance of Sb_2S_3, constructing hybrid heterostructures based on Sb_2S_3 has been regarded as the most commonly used and effective tactic.[13–15] Li

[a]School of Pharmaceutical and Chemical Engineering, Taizhou University, Jiaojiang, Zhejiang Province, 318000, PR China. E-mail: hezhicai@tzc.edu.cn; gbhuang973@163.com; wchen@tzc.edu.cn

[b]State Key Laboratory of Organic Electronics and Information Displays, Institute of Advanced Materials (IAM), New Energy Technology Engineering Lab of Jiangsu Province, Nanjing University of Posts and Telecommunications (NUPT), Nanjing, Jiangsu, 210023, P. R. China

[c]School of Mechanical Engineering, Jiangsu University, Zhenjiang, Jiangsu, 212013, P. R. China. E-mail: wmingyuan298@gmail.com

[d]School of Materials Science and Engineering, Jiangsu University, Zhenjiang, 212013, China

† Electronic supplementary information (ESI) available. See DOI: https://doi.org/10.1039/d4ta08841g

et al. constructed a Sb_2S_3@CdS core–shell heterojunction by *in situ* immobilizing CdS nanoparticles on the surface of Sb_2S_3 in a solvothermal environment. Ascribed to the efficient charge separation based on the formation of van der Waals force and Sb–S–Cd bonding throughout the heterogeneous interface between CdS and Sb_2S_3, the resultant Sb_2S_3@CdS heterostructured sample exhibited highly enhanced activity toward simulated sunlight-driven Cr^{6+} reduction and decomplexation of complexed Cr^{3+} under weakly acidic conditions.[14] Garg *et al.* fabricated a g-C_3N_4/Sb_2S_3 heterojunction photocatalyst with varying weight ratios by a hydrothermal reaction. Among the samples, the optimal g-C_3N_4/Sb_2S_3 composite exhibited the highest photocatalytic performance for tetracycline degradation under natural sunlight because of the rapid charge separation and transfer across the hetero-interface.[15]

Zinc indium sulfide ($ZnIn_2S_4$) has the features of excellent optical properties, strong visible-light harvesting ability and highly catalytic stability, making it a promising material for photocatalytic applications.[16–18] Besides, $ZnIn_2S_4$ with a two-dimensional structure possessing a large active surface area could provide sufficient active sites for various photocatalytic reactions.[19,20] More importantly, previous investigations indicated that the integration of $ZnIn_2S_4$ and Sb_2S_3 would significantly improve the charge migration efficiency based on the construction of a tightly bonded interface and well-matched band structures between $ZnIn_2S_4$ and Sb_2S_3.[21,22] In recent research, Xiao *et al.* synthesized hierarchical Sb_2S_3/$ZnIn_2S_4$ heterostructures using the hydrothermal method, which exhibit highly efficient activities toward both photocatalytic hydrogen production and tetracycline hydrochloride photodegradation.[21] Li *et al.* have also formed a $ZnIn_2S_4$@Sb_2S_3 heterojunction with an enhanced photocatalytic hydrogen evolution activity *via* an oil bath method.[22] The above prepared binary heterostructures demonstrate their potential for hydrogen production and pollutant photodegradation. However, the photocatalytic activity, the reaction pathways, and the effect of sulfur vacancies on nitrogen photofixation using Sb_2S_3@$ZnIn_2S_4$ core–shell heterostructures are still unclear. Hence, it is still necessary to build chemically bonded interface modulated Sb_2S_3@$ZnIn_2S_4$ core–shell heterostructures to achieve highly efficient activity of nitrogen photofixation and simultaneously demystify the charge migration direction and the catalytic mechanism of nitrogen photofixation.

To establish high-quality Sb_2S_3 based photocatalytic systems with efficient performance and excellent stability for highly efficient nitrogen photofixation, herein, Sb_2S_3@$ZnIn_2S_4$ core–shell heterostructures with interfacial chemical bonds were successfully fabricated by *in situ* growth of $ZnIn_2S_4$ nanosheets onto Sb_2S_3 nanorods. A nitrogen photofixation experiment under ambient conditions was conducted to evaluate the catalytic performance of the fabricated Sb_2S_3@$ZnIn_2S_4$ photocatalyst by utilizing a Xe lamp as the light source. The results indicated that the optimal Sb_2S_3@$ZnIn_2S_4$ photocatalyst with addition of 75 mg of Sb_2S_3 nanorods achieved the highest photocatalytic activity for ammonia production from nitrogen, with an activity of 1.88 and 7.19 times higher than those of relevant $ZnIn_2S_4$ and Sb_2S_3, respectively. The obvious activity improvement in the Sb_2S_3@$ZnIn_2S_4$ core–shell heterostructures can be attributed to synergistic collaboration of interfacial chemical bonds and an internal electric field, which can greatly accelerate charge transfer across the hetero-interface between $ZnIn_2S_4$ and Sb_2S_3, as evidenced by experimental investigations and density functional theory calculations. The S-scheme charge migration mechanism was verified by electron paramagnetic resonance (EPR), nitroblue tetrazolium (NBT) transformation experiments, *in situ* irradiated X-ray photoelectron spectroscopy (ISI-XPS), and noble metal loading.

Experimental section

Preparation of materials

Synthesis of Sb_2S_3 nanorods. Sb_2S_3 nanorods were prepared by a solvothermal reaction according to the method described in previous literature.[11] Typically, $SbCl_3$ (3 mmol, 0.684 g) and thiourea (18 mmol, 1.370 g) were added into 80 mL ethylene glycol (EG) to obtain a clear solution by magnetic stirring for 30 min. Then, the above solution was poured into a 100 mL Teflon-lined autoclave and reacted at 180 °C for 10 h. The resultant black precipitate was washed with deionized water two times and absolute ethanol three times.

Synthesis of the Sb_2S_3@$ZnIn_2S_4$ heterostructured catalyst. Sb_2S_3@$ZnIn_2S_4$ nanocomposites with core–shell heterostructures were synthesized by *in situ* growth of $ZnIn_2S_4$ nanosheets onto Sb_2S_3 nanorods. Typically, a certain amount of as-synthetic Sb_2S_3 nanorods was suspended in a mixed solvent consisting of 32 mL deionized water and 8 mL glycerol. Then, $ZnCl_2$ (1 mmol, 0.136 g), $In(NO_3)_3$ (2 mmol, 0.602 g), and thioacetamide (6 mmol, 0.451 g) were gradually dissolved in the above suspension. Subsequently, the mixture was transferred to a 50 mL Teflon-lined autoclave and reacted at 120 °C for 2 h. After naturally cooling down to room temperature, the powdery precipitate was washed with absolute ethanol three times. Finally, the as-obtained Sb_2S_3@$ZnIn_2S_4$ precipitate was dried at 60 °C for 6 h. According to the added amount of Sb_2S_3 nanorods, the heterostructured samples were denoted as Sb_2S_3@$ZnIn_2S_4$-*x* (*x* represents the added amount of Sb_2S_3, *viz.*, 25, 50, 75, and 100 mg). For comparison, pure $ZnIn_2S_4$ was prepared under the same reaction condition just without the addition of Sb_2S_3 nanorods.

Characterization

A powder X-ray diffractometer (XRD, Bruker D2 Phaser Diffractometer) equipped with a monochromatic Cu K_α generator was used to examine crystalline structures. Field-emission scanning electron microscopy (FESEM, ZEISS GeminiSEM 300), transmission electron microscopy (TEM, FEI Titan Cubed Themis G2 300), and high-angle annular dark field scanning TEM (HAADF-STEM, FEI Titan Cubed Themis G2 300) were carried out to observe the morphologies, structures, and elements. Nitrogen adsorption–desorption measurements (Micromeritics ASAP 2460) were performed to record Brunauer–Emmett–Teller (BET) surface areas and pore-diameter distribution. X-ray photoelectron spectroscopy (XPS, ESCALAB 250Xi) and *in situ*

irradiated XPS (ISI-XPS, ESCALAB 250Xi) with monochromatic Al K_α radiation were conducted to analyze the element compositions and electron transfer in the measured samples. Fourier transform infrared (FT-IR) spectra of samples were recorded using a Thermo Fisher Nicolet IS50 infrared spectrometer. Ultraviolet–visible diffuse reflectance spectra (UV-vis DRS, U-4100) were recorded to acquire optical properties with $BaSO_4$ as a reference. Electron paramagnetic resonance (EPR) was measured on a Bruker A300 EPR spectrometer. The photoluminescence (PL) and time-resolved PL (TRPL) spectra were recorded on an F-4600 fluorescence spectrophotometer at room temperature. The photoelectrochemical measurements including transit photocurrent response and electrochemical impedance spectra (EIS) were performed in Na_2SO_4 aqueous solution (0.5 M) under irradiation of a 300 W Xe lamp on a CHI760E electrochemical workstation using a three-electrode electrochemical system, in which a Pt wire and Ag/AgCl electrode were used as the counter electrode and reference electrode, respectively. The details about the theoretical calculations are shown in the ESI† and the atomic structure diagram used in the calculation could be found in Fig. S1.†

Photocatalytic activity

Photocatalytic activity toward ammonia production by nitrogen photofixation was performed in a homemade catalytic system at room temperature and atmospheric pressure under irradiation of a 300 W Xe lamp (PerfectLight). Typically, 50 mg photocatalyst was ultrasonically dispersed in 50 mL deionized water including 1 mL methanol as the hole scavenger. Prior to the catalytic reaction, the suspension was bubbled for 30 min by nitrogen at a flow rate of 100 mL min^{-1}. At given irradiation time intervals, the irradiated suspension was extracted and separated using a polyether sulfone filter to obtain the supernatant. The concentration of produced ammonia was quantitatively analyzed using Nessler's reagent with a UV-visible absorption spectrophotometer (UVmini-1280, Shimadzu). The produced NH_3 was further verified by ion chromatography (Thermo Scientific Aquion) coupled with an NH_3-selective electrode (Bante 931-NH_3).

Results and discussion

The fabrication of Sb_2S_3@$ZnIn_2S_4$ core–shell heterostructures involved two steps, that is, solvothermal synthesis of Sb_2S_3 nanorods and the construction of a heterogeneous interface by *in situ* growth of $ZnIn_2S_4$ nanosheets on Sb_2S_3 nanorods (Fig. 1a). First, under a solvothermal environment, the precursor in EG gradually nucleated and then crystallized to generate Sb_2S_3 nanorods by orientation growth. The morphology of the resultant Sb_2S_3 nanorods was revealed using a field-emission scanning electron microscope (FESEM). Fig. 1b depicts the one-dimensional structure of the as-prepared Sb_2S_3 sample with a smooth surface and its length irregularly varied within several microns. Then, through a solvothermal process, the produced $ZnIn_2S_4$ crystal nucleus tended to immobilize on the Sb_2S_3 surface and further grew into nanosheets; simultaneously $ZnIn_2S_4$ nanosheets grew along the surface of the Sb_2S_3 nanorods to form a tight heterogeneous interface between Sb_2S_3 nanorods and $ZnIn_2S_4$ nanosheets, namely, the fabrication of Sb_2S_3@$ZnIn_2S_4$ core–shell heterostructures. The successful decoration of $ZnIn_2S_4$ nanosheets on Sb_2S_3 nanorods could be observed by FESEM. As shown in Fig. 1d and S2a–c,† all the Sb_2S_3@$ZnIn_2S_4$ samples exhibited core–shell heterostructures with a rough surface, which clearly proved that the Sb_2S_3 nanorods with a smooth surface were tightly covered by $ZnIn_2S_4$ nanosheets. These close heterogeneous contacts would act as high-speed channels to promote the separation of photogenerated electrons and holes, thus improving the photocatalytic activity. It is worth noting that, when a small amount (25 mg) of Sb_2S_3 nanorods was introduced into the reaction system, some of the $ZnIn_2S_4$ nanosheets would agglomerate to form microsphere-like assemblies due to the lack of enough Sb_2S_3 nanorods to act as supporting carriers (Fig. S2a†). With the increase of the added amount of Sb_2S_3 nanorods, the $ZnIn_2S_4$ nanosheet assembly gradually disappeared, leaving only the Sb_2S_3@$ZnIn_2S_4$ core–shell heterostructures. Therefore, it is important to optimize the added amount of Sb_2S_3 nanorods to acquire suitable Sb_2S_3@$ZnIn_2S_4$ core–shell heterostructures.

To better elucidate the *in situ* growth of $ZnIn_2S_4$ nanosheets on Sb_2S_3 nanorods and the construction of Sb_2S_3@$ZnIn_2S_4$ core–shell heterostructures, transmission electron microscope (TEM), high-resolution TEM (HRTEM) and high-angle annular dark field scanning TEM (HAADF-STEM) characterization of the Sb_2S_3@$ZnIn_2S_4$-75 was performed to obtain the microstructure information. The TEM images revealed that the $ZnIn_2S_4$ nanosheets exhibited a sheet-like morphology, and the heterogeneous structures were observed throughout these ultrathin nanosheets tightly decorated on the Sb_2S_3 nanorods (Fig. 1e and f). The above results confirmed that the Sb_2S_3@$ZnIn_2S_4$ heterostructures were heterogeneous hybrid systems with tight interface contacts as opposed to the physical mixtures of the individual Sb_2S_3 and $ZnIn_2S_4$ phases. The HRTEM image (Fig. 1g) showed clear lattice fringes with the interplanar distances of 0.278 and 0.412 nm, belonging to the (006) crystal plane of hexagonal $ZnIn_2S_4$ and the (221) crystal plane of orthotropic stibnite Sb_2S_3, respectively. Fig. 1h illustrates the HAADF image of the Sb_2S_3@$ZnIn_2S_4$-75 sample. It was worth noting that ultrathin $ZnIn_2S_4$ nanosheets were evenly dispersed and hierarchically wrapped on the surface of Sb_2S_3 nanorods to build core–shell catalytic systems. The elemental mapping images of the Sb_2S_3@$ZnIn_2S_4$-75 sample (Fig. 1i–l) clearly reveal that all the elements with uniform distribution corresponded to the measured sample region, revealing the successful construction of the Sb_2S_3@$ZnIn_2S_4$ hybrid sample. The microstructure observation demonstrated that Sb_2S_3@$ZnIn_2S_4$ core–shell heterostructures effectively established good interfacial contacts through obvious morphological changes of $ZnIn_2S_4$ from assembly to ultrathin nanosheets. These ultrathin nanosheets decorated on the contacted interfaces between Sb_2S_3 and $ZnIn_2S_4$ could not only facilitate the rapid separation of photogenerated hole–electron pairs, but also cause more exposure of additional active sites and this improves the reaction sites,

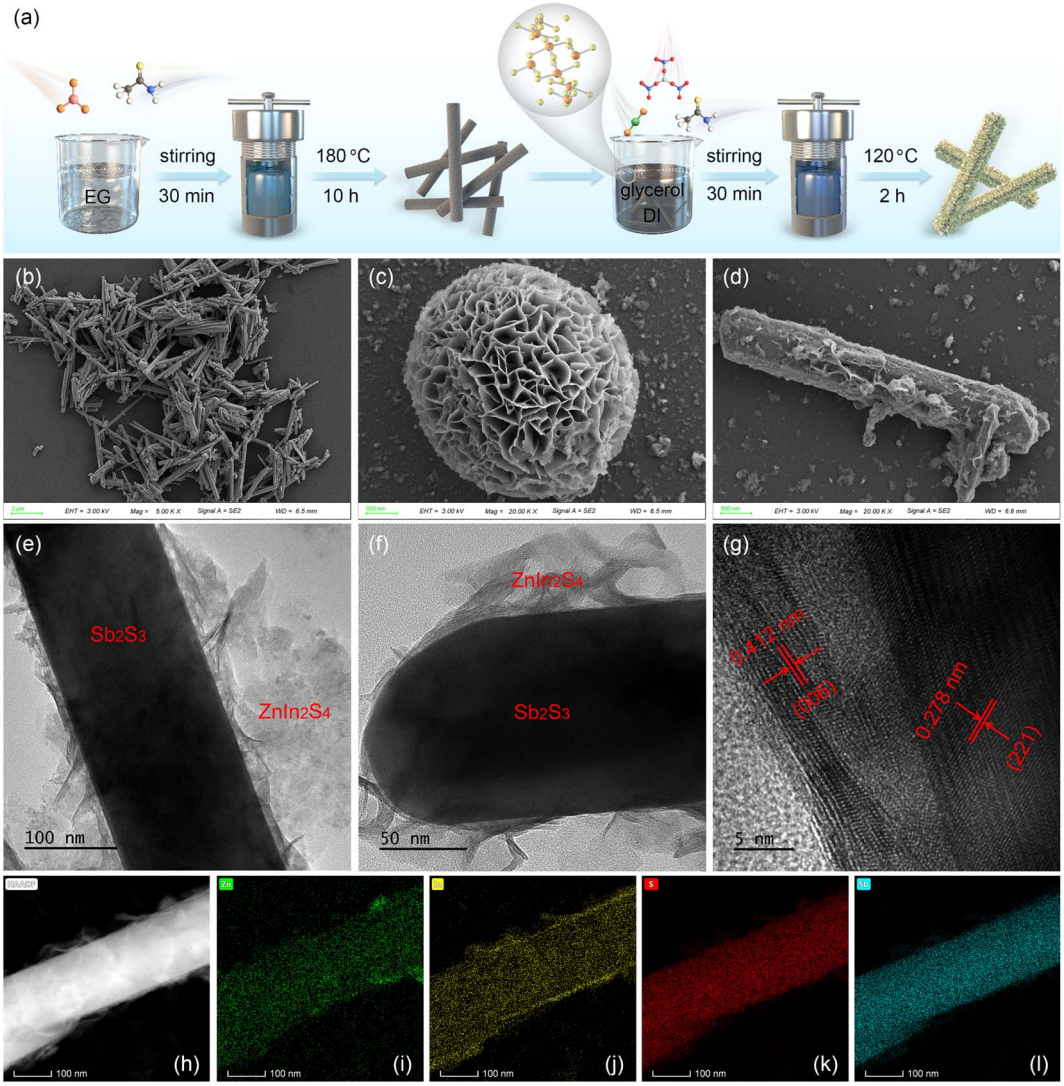

Fig. 1 (a) Schematic diagram of the synthetic process of Sb_2S_3@$ZnIn_2S_4$ core–shell heterostructures. SEM images of (b) Sb_2S_3, (c) $ZnIn_2S_4$, and (d) Sb_2S_3@$ZnIn_2S_4$-75. (e and f) TEM, (g) HRTEM, (h) HAADF, and (i–l) elemental mapping images of the Sb_2S_3@$ZnIn_2S_4$-75 sample.

which is beneficial for improving the photocatalytic performance toward nitrogen photofixation.

The powder X-ray diffraction (XRD) technique was used to analyze the phase structures of the different samples, as shown in Fig. 2a. The characteristic diffraction peaks of Sb_2S_3 agreed well with the standard card of the orthorhombic phase (JCPDS No. 42-1393).[11] The XRD patterns of $ZnIn_2S_4$ were in good accordance with those of the hexagonal phase (JCPDS No. 65-2023).[23] After solvothermally decorating $ZnIn_2S_4$ nanosheets on the Sb_2S_3 surface, the synthesized Sb_2S_3@$ZnIn_2S_4$ core–shell heterostructures with different amounts of Sb_2S_3 added exhibited integrated XRD patterns of Sb_2S_3 and $ZnIn_2S_4$. The diffraction intensity belonging to Sb_2S_3 increased obviously with increasing amount of Sb_2S_3 added into the Sb_2S_3@$ZnIn_2S_4$ core–shell heterostructures, further proving the coexistence and successful combination of Sb_2S_3 and $ZnIn_2S_4$. The above results well supported the conclusion of SEM/TEM observation. No other impurities were observed, revealing the high purity of the synthesized samples. The optical absorption ability of pure $ZnIn_2S_4$, bare Sb_2S_3 and their Sb_2S_3@$ZnIn_2S_4$ core–shell heterostructures was checked by ultraviolet–visible diffuse reflectance spectroscopy (UV-vis DRS), as shown in Fig. 2b. Noticeably, pure $ZnIn_2S_4$ exhibited a certain light absorption capacity with an absorption threshold of around 560 nm, while bare Sb_2S_3 had a strong light absorption ability and could absorb most of the irradiated light throughout the ultraviolet to visible light region. Such an excellent optical absorption ability of Sb_2S_3 signified that it could probably be utilized to improve the light harvesting ability of $ZnIn_2S_4$. Indeed, after the construction of Sb_2S_3@$ZnIn_2S_4$ samples, all the core–shell heterostructures showed improved light absorption intensity in the measured range with increasing Sb_2S_3 content. Moreover, compared to pure $ZnIn_2S_4$, all Sb_2S_3@$ZnIn_2S_4$ core–shell heterostructures had a slight red shift toward the longer wavelength region upon the introduction of Sb_2S_3, which revealed that a certain interaction between Sb_2S_3 and $ZnIn_2S_4$ was

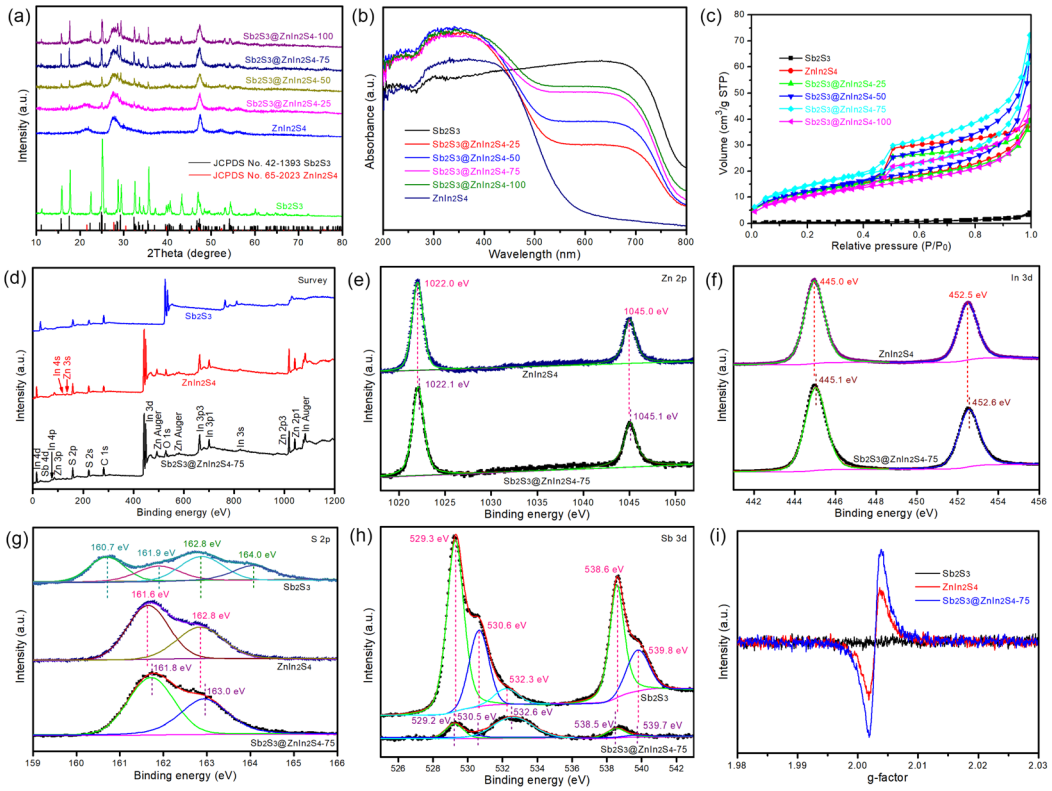

Fig. 2 (a) XRD patterns, (b) UV-vis DRS, and (c) N_2 adsorption/desorption curves of pure $ZnIn_2S_4$, bare Sb_2S_3 and their Sb_2S_3@$ZnIn_2S_4$ heterostructures. XPS data: (d) survey spectra, (e) Zn 2p, (f) In 3d, (g) S 2p, and (h) Sb 3d. (i) EPR spectra of pure $ZnIn_2S_4$, bare Sb_2S_3 and the Sb_2S_3@$ZnIn_2S_4$-75 heterostructures.

formed due to the surface coverage of Sb_2S_3 nanorods with $ZnIn_2S_4$ nanosheets. The improved light harvesting efficiency of $ZnIn_2S_4$ in the measured region by coupling with Sb_2S_3 meant that more photogenerated charges were produced and then participated in the photocatalytic reaction, giving rise to the activity enhancement of nitrogen photofixation.

The specific surface area and porosity of pure $ZnIn_2S_4$, bare Sb_2S_3 and their Sb_2S_3@$ZnIn_2S_4$ core–shell heterostructures were studied through N_2 adsorption/desorption tests. As shown in Fig. 2c, the isotherms of the measured samples were characteristic of type IV, with a type H3 adsorption hysteresis loop, indicating the presence of mesoporous structures.[24,25] Additionally, the macroporous structures in the samples were also recorded as indicated by pore size distributions (Fig. S3†), which could probably be ascribed to the slit holes formed between $ZnIn_2S_4$ nanosheets. The Brunauer–Emmett–Teller (BET) specific surface areas (SSAs) of pure $ZnIn_2S_4$ and bare Sb_2S_3 were determined to be 45.34 and 2.01 $m^2\ g^{-1}$, respectively. As shown in Table S1,† after the $ZnIn_2S_4$ nanosheets were anchored on the Sb_2S_3 nanorods, the BET SSA and total pore volume gradually increased for the Sb_2S_3@$ZnIn_2S_4$ core–shell heterostructures with increasing Sb_2S_3 addition until the addition amount of Sb_2S_3 reached 75 mg. Further increasing the amount of Sb_2S_3 nanorods added would lead to a decrease in the BET SSA. The large SAA of the Sb_2S_3@$ZnIn_2S_4$-75 heterostructure usually provided more surface active sites and probably increased the photocatalytic reactivity.

To investigate the chemical states and interfacial interaction between Sb_2S_3 and $ZnIn_2S_4$, X-ray photoelectron spectroscopy (XPS) tests were conducted. As observed in Fig. 2d, the XPS survey spectrum of the Sb_2S_3@$ZnIn_2S_4$-75 heterostructure revealed the existence of Zn, In, S, and Sb elements, providing evidence of coupling between Sb_2S_3 and $ZnIn_2S_4$. As shown in Fig. 2e and f, the pure $ZnIn_2S_4$ sample had two characteristic binding energies centered at 1022.0 and 1045.0 eV in Zn 2p and 445.0 and 452.5 eV in In 3d, belonging to the Zn $2p_{3/2}$ and Zn $2p_{1/2}$ states of Zn^{2+} and the In $3d_{5/2}$ and In $3d_{3/2}$ states of In^{3+}, respectively.[26,27] From the high-resolution spectrum of S 2p (Fig. 2g), the asymmetric S 2p peak of bare Sb_2S_3 could be deconvoluted into four peaks located at 160.7, 161.9, 162.8, and 164.0 eV. The first two peaks located at 160.7 and 161.9 eV were probably ascribed to S bonded with Sb in a double bond. The two remaining peaks centered at 162.8 and 164.0 eV were assigned to S bonded with Sb by a single bond. Pure $ZnIn_2S_4$ also exhibited two peaks with binding energies of 161.6 and 162.8 eV, which corresponded to S $2p_{3/2}$ and S $2p_{1/2}$, respectively.[28,29] After the coupling of $ZnIn_2S_4$ with Sb_2S_3, the core level of Zn, In, and S species in the Sb_2S_3@$ZnIn_2S_4$-75 heterostructure obviously moved in the high binding energy direction. The slight positive shift of these peaks was also attributed to the interfacial charge transfer of $ZnIn_2S_4$ and Sb_2S_3. Bare Sb_2S_3 was fitted with five peaks (Fig. 2h). The peaks at 529.3 eV (Sb $3d_{5/2}$), 538.6 eV (Sb $3d_{3/2}$), 530.6 eV (Sb $3d_{5/2}$) and 539.8 eV (Sb $3d_{3/2}$) represented the different bonding states of Sb with S.[30] There

was an extra peak at 532.3 eV, which was ascribed to oxygen-containing functional groups absorbed on the surface of the sample. The abovementioned Sb species belonging to Sb $3d_{5/2}$ and Sb $3d_{5/2}$ shifted toward the lower binding energy region upon fabricating the heterostructure.[31] The above results verified the M–S–Sb (M = Zn and In) bond formed at the heterogeneous interface of Sb_2S_3@$ZnIn_2S_4$, which induced strong interfacial interaction between these two components with free electron migration from $ZnIn_2S_4$ to Sb_2S_3. This strong interface interaction and charge redistribution between $ZnIn_2S_4$ and Sb_2S_3 probably induce the formation of an internal electric field within Sb_2S_3@$ZnIn_2S_4$ heterostructures. As shown in Fig. 2i, both $ZnIn_2S_4$ and Sb_2S_3@$ZnIn_2S_4$-75 had a Lorentzian line shape emerging at $g = 2.002$, verifying the formation of sulfur vacancies in these two samples.[32]

The photocatalytic performance of bare Sb_2S_3, pure $ZnIn_2S_4$, and the Sb_2S_3@$ZnIn_2S_4$ samples toward nitrogen photofixation was investigated by adding methanol as a sacrificial agent to capture photogenerated holes under visible light irradiation, as shown in Fig. 3a. Control experiments under different experimental conditions were carried out with the Sb_2S_3@$ZnIn_2S_4$-75 sample (Fig. S4 and S5†). There was no NH_4^+ produced in the absence of the visible light, indicating that the light irradiation was the essential driving force for the nitrogen photofixation. Notably, the Sb_2S_3@$ZnIn_2S_4$-75 sample exhibited significantly decreased activity toward nitrogen photofixation when N_2 was replaced with Ar, confirming that N_2 was indeed the N source of the photofixation reaction. Without the introduction of methanol, the catalytic activity toward nitrogen photofixation was greatly suppressed because added methanol into the catalytic system as a scavenger of photogenerated holes could effectively inhibit the recombination of photogenerated holes and electrons and actively improve the utilization rate of photogenerated electrons for the nitrogen reduction reaction. Apparently, bare Sb_2S_3 nanorods exhibited low ammonia production activity due to low charge migration efficiency. By contrast, $ZnIn_2S_4$ exhibited suitable photocatalytic nitrogen photofixation activity and it reached 8.51 ± 1.29 mg L^{-1} for ammonia production after visible light irradiation for 40 min. The photocatalytic performance toward nitrogen photofixation dependence on the Sb_2S_3 content was in-depth explored. After the Sb_2S_3@$ZnIn_2S_4$ core–shell heterostructures were constructed, all Sb_2S_3@$ZnIn_2S_4$ hybrid samples possessed improved photocatalytic activity. The improvement of the photocatalytic performance of Sb_2S_3@$ZnIn_2S_4$ hybrid samples was probably due to the efficient charge migration across the heterogeneous interface between Sb_2S_3 and $ZnIn_2S_4$. Notably, photocatalytic ammonia production activity first increased and then decreased in the Sb_2S_3@$ZnIn_2S_4$ hybrid systems with the increase of Sb_2S_3 content. Among all the Sb_2S_3@$ZnIn_2S_4$ hybrid samples, the optimized Sb_2S_3@$ZnIn_2S_4$-75 sample showed the highest photocatalytic activity, and an ammonia concentration of 15.96 ± 0.97 mg L^{-1} could be produced after 40 min of visible light irradiation, which was around 7.19 and 1.88 times higher than those of bare Sb_2S_3 and pure $ZnIn_2S_4$, respectively. The produced NH_3 over Sb_2S_3@$ZnIn_2S_4$-75 was further verified by ion chromatography coupled with an NH_3-selective electrode. The concentrations from ion chromatography and the NH_3-selective electrode were determined to be 9.30 and 8.50 mg L^{-1}, respectively. A higher Sb_2S_3 content in the Sb_2S_3@$ZnIn_2S_4$-100 sample resulted in the decrease of photocatalytic ammonia production activity, which was probably due to the decreased concentration of interfacial contacts and active sites as evidenced by SEM observation and BET measurement. Yang *et al.*

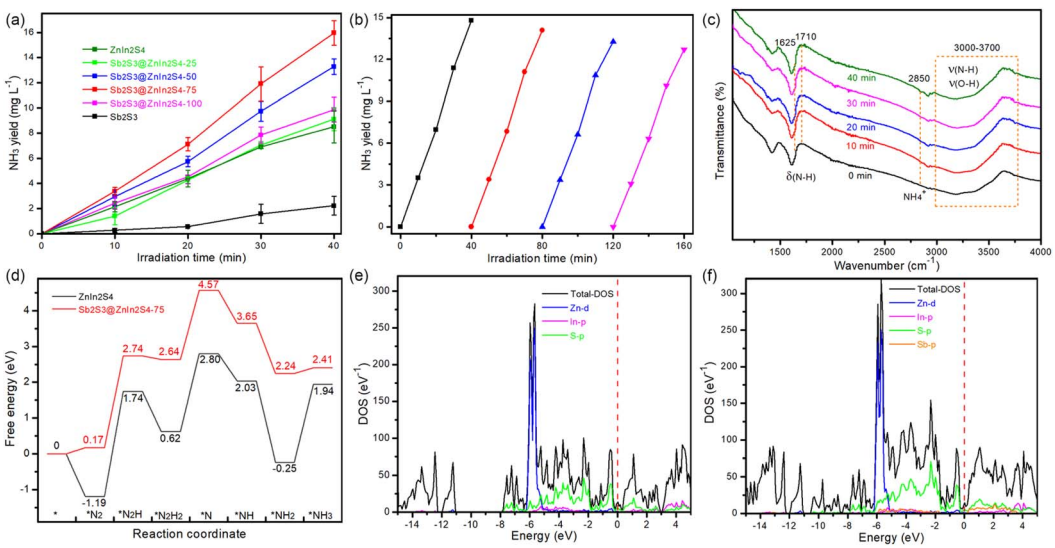

Fig. 3 (a) Photocatalytic ammonia production activity over bare Sb_2S_3, pure $ZnIn_2S_4$, and the Sb_2S_3@$ZnIn_2S_4$ samples with the addition of methanol as the sacrificial agent under visible light irradiation. (b) Recycling runs toward N_2 photofixation for ammonia production over the Sb_2S_3@$ZnIn_2S_4$-75 sample. (c) FTIR spectra during the N_2 photofixation process over the Sb_2S_3@$ZnIn_2S_4$-75 sample. (d) Gibbs free energy diagrams of the main reactions during N_2 photofixation over $ZnIn_2S_4$ and Sb_2S_3@$ZnIn_2S_4$-75 samples. Density of states (DOS) of (e) $ZnIn_2S_4$ and (f) Sb_2S_3@$ZnIn_2S_4$ samples.

revealed that the nitrogen reduction reaction could generate more reactive intermediates to induce photocatalytic urea production by the activation and oxidation of CH_3OH over the Pt cluster-decorated TiO_2 catalyst.[33] To reveal the possibility of the photocatalytic urea production, the produced concentration of urea was measured by the diacetyl monoxime method through UV-vis absorption spectroscopy at a characteristic wavelength of 525 nm (Fig. S6†). No obvious improvement of absorption intensity could be observed with extended irradiation time, indicating that the Sb_2S_3@$ZnIn_2S_4$-75 sample cannot produce urea although methanol was added into the reaction system during the nitrogen photofixation process. The photocatalytic stability of the Sb_2S_3@$ZnIn_2S_4$ heterostructures was evaluated through recycling runs toward N_2 photofixation for ammonia production over the Sb_2S_3@$ZnIn_2S_4$-75 sample (Fig. 3b). During the recycling runs, the Sb_2S_3@$ZnIn_2S_4$-75 sample displayed a slight decrease in activity. After four consecutive recycling reactions, the Sb_2S_3@$ZnIn_2S_4$-75 sample still retained 79.6% of initial activity, indicating relatively good stability for practical applications. Furthermore, FT-IR spectra of the Sb_2S_3@$ZnIn_2S_4$-75 sample with different irradiation times are shown in Fig. 3c. These broad absorption bands within 3000–3700 cm^{-1} from different N_2 photofixation times could be ascribed to the stretching mode of O–H and N–H functional groups.[34] The characteristic absorption peak at 2850 cm^{-1} is due to the stretching vibration of NH_4^+.[35] Notably, this absorption peak at 2850 cm^{-1} is only observed in the irradiated samples, which revealed that Sb_2S_3@$ZnIn_2S_4$-75 exhibited visible-light driven catalytic activity towards N_2 photofixation. The absorption peaks at 1625 and 1710 cm^{-1} verify the presence of N–H bending mode.[36] The above results indicate that the N_2 photofixation reaction can be successfully achieved by Sb_2S_3@$ZnIn_2S_4$-75 under visible-light irradiation. Moreover, to further reveal the catalytic mechanism of N_2 photofixation, hydrazine, as an important intermediate product during the N_2 photofixation process, was detected by the Watt–Chrisp method (Fig. S7†).[37] Obviously, no by-product hydrazine in the residual solutions was detected. The above results indicated that the N_2 photofixation pathways toward ammonia production were most likely to follow the associative distal mechanism because of the presence of a N–H bond and NH_4^+ but the absence of N_2H_4. To further reveal the pathways of N_2 photofixation, the corresponding Gibbs free energies (ΔG) for each step of the N_2 photofixation process were calculated, as shown in Fig. 3d. Notably, the $*N_2H_2$ to *N step exhibited a high energy barrier, indicating that this was the rate-limiting step in the N_2 photofixation. In addition, the Sb_2S_3@$ZnIn_2S_4$ samples exhibited a smaller energy barrier than $ZnIn_2S_4$, which was beneficial for N_2 photofixation for ammonia production. The observed phenomenon can be attributed to the increase in the number of DOS peaks near the Fermi level on the right side for Sb_2S_3@$ZnIn_2S_4$, primarily originating from the contribution of the p orbitals of Sb, as shown in Fig. 3e and f. This increase enhances the conductivity, thereby facilitating the activation of N_2. Consequently, the energy barrier for the conversion of N_2 to NH_3 is significantly reduced for Sb_2S_3@$ZnIn_2S_4$.

To explore the origin of the boosted photocatalytic performance of Sb_2S_3@$ZnIn_2S_4$ heterostructures, the migration behaviors of photogenerated charges were systematically investigated. First, the Mott–Schottky (M–S) curves were recorded to reveal the conduction band potential (E_{CB}) of the semiconductors. In Fig. 4a and b, the M–S curves revealed that both Sb_2S_3 and $ZnIn_2S_4$ possessed positive slopes, indicating n-type semiconductor features.[38,39] The flat-band potential (E_{fb}) of Sb_2S_3 and $ZnIn_2S_4$ was appropriately −0.75 and −1.43 V *versus* Ag/AgCl, respectively. As the E_{fb} of n-type semiconductors is about 0.1 V positive compared to E_{CB}, the CB positions of Sb_2S_3 and $ZnIn_2S_4$ were determined to be −0.25 and −0.83 V *versus*

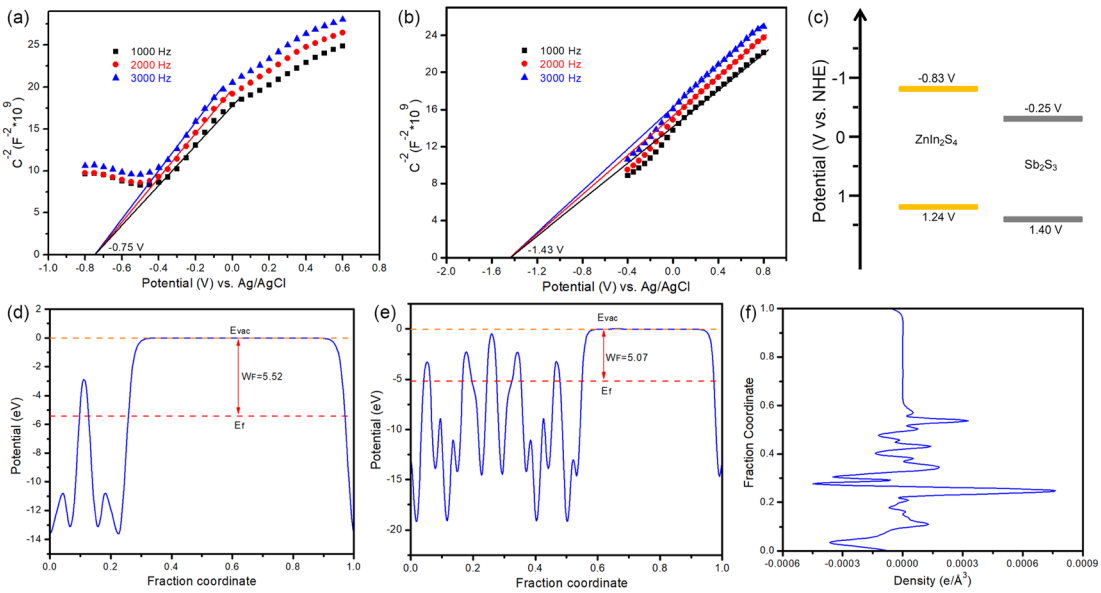

Fig. 4 Mott–Schottky curves of (a) Sb_2S_3 and (b) $ZnIn_2S_4$. (c) Band structures of Sb_2S_3 and $ZnIn_2S_4$. Calculated average potential profile along the *Z* axis of (d) Sb_2S_3 and (e) $ZnIn_2S_4$. (f) Plane average electron density difference of Sb_2S_3@$ZnIn_2S_4$.

the normal hydrogen electrode (NHE), respectively.[40] Combined with their band gap (E_g) values (Fig. S8†), the band structure diagrams of Sb_2S_3 and $ZnIn_2S_4$ are shown in Fig. 4c. Apparently, the staggered and matched band alignment between Sb_2S_3 and $ZnIn_2S_4$ was established, which was conducive to fabricating type II or S-scheme heterostructures. Subsequently, the work function (Φ), a key physical parameter to determine free electron transfer within the heterojunction, was calculated by DFT. The Φ of Sb_2S_3 was about 5.52 eV (Fig. 4d), which was obviously bigger than that of $ZnIn_2S_4$ (5.07 eV) (Fig. 4e). Therefore, upon the construction of Sb_2S_3@$ZnIn_2S_4$ heterostructures, the free electrons in $ZnIn_2S_4$ with a high Fermi level would spontaneously diffuse to Sb_2S_3 with a low Fermi level through the heterogeneous interface between Sb_2S_3 and $ZnIn_2S_4$ to equilibrate the Fermi level of these two components.[41] This free electron redistribution cause heterogeneous interface near the sides of Sb_2S_3 and $ZnIn_2S_4$ forming an electron accumulation layer with negative charge and an electron depletion layer with positive charge, respectively, as evidenced by the charge density difference (Fig. 4f and S9†). As a result, this interfacial charge distribution led to the formation of an internal electric field pointing from $ZnIn_2S_4$ to Sb_2S_3, which effectively promoted rapid migration of photogenerated charges across the heterogeneous interfaces and thus improved catalytic performance toward N_2 photofixation.[42]

To prove the migration direction of photogenerated charges within Sb_2S_3@$ZnIn_2S_4$ heterostructures, systematical characterization studies, including electron paramagnetic resonance (EPR), nitroblue tetrazolium (NBT) transformation experiments, *in situ* irradiated X-ray photoelectron spectroscopy (ISI-XPS), and noble metal loading, were carried out. As shown in Fig. 5a, the EPR signal of DMPO–$^{\cdot}O_2^-$ was detected in the suspension of Sb_2S_3@$ZnIn_2S_4$-75 under visible light irradiation and its intensity gradually increased with extended irradiation time, indicating that the Sb_2S_3@$ZnIn_2S_4$-75 sample was capable of producing $^{\cdot}O_2^-$.[43] The produced $^{\cdot}O_2^-$ was further analyzed through NBT transformation experiments (Fig. 5b). Apparently, the absorption spectral intensity of NBT decreased as the radiation time increased when the Sb_2S_3@$ZnIn_2S_4$-75 sample was introduced, indicating that $^{\cdot}O_2^-$ indeed appeared in irradiated Sb_2S_3@$ZnIn_2S_4$-75 and simultaneously NBT was successfully consumed by the produced $^{\cdot}O_2^-$.[44] Interestingly, the E_{CB} of

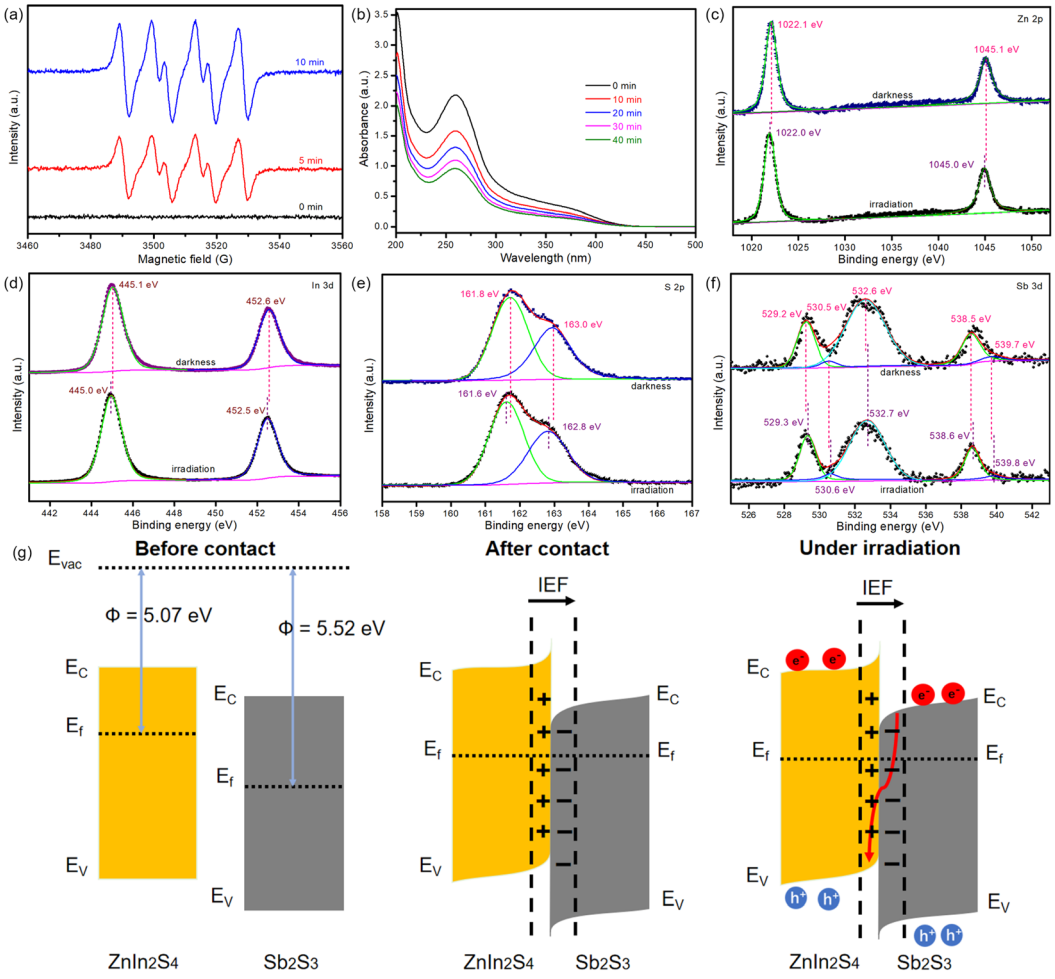

Fig. 5 (a) EPR spectra and (b) time-dependent absorption peak of NBT over the Sb_2S_3@$ZnIn_2S_4$-75 sample. ISI-XPS data: (c) Zn 2p, (d) In 3d, (e) S 2p, and (f) Sb 3d. (g) Schematic illustration of internal electric field formation and the S-scheme charge transfer pathway at the interface of Sb_2S_3@$ZnIn_2S_4$ under light irradiation.

Sb_2S_3 does not meet the conversion requirements of $O_2/{}^{\bullet}O_2^-$ (−0.33 V),[45] suggesting that ${}^{\bullet}O_2^-$ does not originate from the oxygen reduction reaction between O_2 and E_{CB} of Sb_2S_3. Therefore, based on the above results and analyses, we could draw the conclusion that the Sb_2S_3@$ZnIn_2S_4$ sample followed an S-scheme rather than a type II charge separation mechanism. ISI-XPS was performed to directly verify the S-scheme charge separation mechanism within the Sb_2S_3@$ZnIn_2S_4$ sample. As shown in Fig. 5c–f, the results from ISI-XPS indicated that Sb_2S_3@$ZnIn_2S_4$-75 exhibited smaller binding energy in the regions of Zn 2p, In 3d, and S 2p and bigger binding energy in Sb 3d when exposed to light irradiation than those in the darkness. These results indicated that the photogenerated electrons in the CB of Sb_2S_3 were injected into $ZnIn_2S_4$, further verifying the S-scheme charge migration mechanism.[46,47] Such a charge migration path, driven by the internal electric field between Sb_2S_3 and $ZnIn_2S_4$, convincingly confirms the successful formation of S-scheme heterostructures (Fig. 5g). The migration direction of photogenerated charge was traced by the noble metal deposition method.[48] It could be noticed that noble Au was tightly loaded onto the surface of $ZnIn_2S_4$ when the Sb_2S_3@$ZnIn_2S_4$-75 sample was used as the photocatalyst (Fig. S10†), revealing that the S-scheme charge migration mechanism was achieved within Sb_2S_3@$ZnIn_2S_4$ samples and photogenerated electrons were accumulated in the CB of $ZnIn_2S_4$.

The efficient charge migration within Sb_2S_3@$ZnIn_2S_4$ heterostructures was explored by photoelectrochemical tests, photoluminescence (PL), time-resolved PL (TRPL), and surface photovoltage (SPV) measurements, as shown in Fig. 6. Compared with bare Sb_2S_3 and pure $ZnIn_2S_4$, the Sb_2S_3@$ZnIn_2S_4$-75 sample with a higher photocurrent intensity (Fig. 6a) and smaller semicircle (Fig. 6b) indicated higher charge transfer and separation efficiency and smaller electrical resistance upon the formation of the heterogeneous interface.[49,50] As shown in Fig. S11,† PL tests revealed Sb_2S_3@$ZnIn_2S_4$-75 could produce lower PL intensity in comparison with pure $ZnIn_2S_4$, indicating either a faster migration process with a shorter lifetime or a slower recombination process with a longer lifetime for the photogenerated electrons.[51] Then, TRPL spectra of the Sb_2S_3@$ZnIn_2S_4$-75 heterostructure and pure $ZnIn_2S_4$ were further recorded to investigate the migration dynamics behavior of photogenerated charge (Fig. 6c). Both Sb_2S_3@$ZnIn_2S_4$-75 and pure $ZnIn_2S_4$ could be fitted with a double exponential function and the corresponding fitting parameters are described in Table S2.† Apparently, the average PL lifetime of $ZnIn_2S_4$ was prolonged from 4.81 to 5.48 ns after coupling with Sb_2S_3. As we know, the short lifetime components (τ_1) represented the nonradiative recombination of the photogenerated electrons captured by the surface defects, and the long lifetime components (τ_2) resulted from the recombination of the free excitons.[52] The increased PL lifetime and decreased PL intensity jointly revealed that the radiative recombination of photogenerated electrons on the excited states of $ZnIn_2S_4$ was significantly suppressed due to the existence of Sb_2S_3 in Sb_2S_3@$ZnIn_2S_4$-75 that could inject photogenerated electrons and

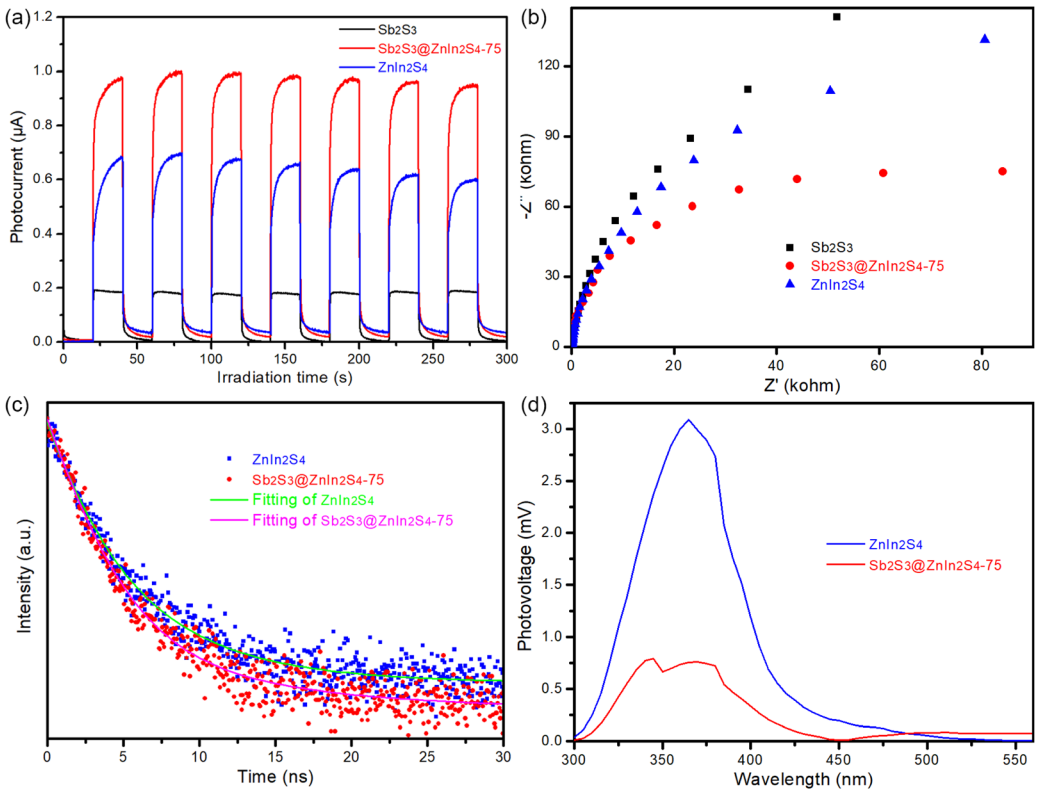

Fig. 6 (a) Photocurrent response, (b) electrochemical impedance spectroscopy (EIS), (c) TRPL, and (d) SPV spectra of the sample.

react with photogenerated holes on the VB of $ZnIn_2S_4$.[53] Fig. 6d shows the SPV spectra of pristine $ZnIn_2S_4$ and Sb_2S_3@$ZnIn_2S_4$-75. Compared with pure $ZnIn_2S_4$, the SPV signal of Sb_2S_3@$ZnIn_2S_4$-75 was obviously decreased, which indicated that more photogenerated holes on $ZnIn_2S_4$ were recombined with injected photogenerated electrons from Sb_2S_3 and thus more photogenerated electrons moved to the surface.[54,55] According to the results, we reached a conclusion that the S-scheme charge transfer gave rise to efficient charge migration across the heterogeneous interface between Sb_2S_3 and $ZnIn_2S_4$.

Conclusion

In conclusion, herein we reported a hydrothermal reaction to synthesize S-scheme Sb_2S_3@$ZnIn_2S_4$ hybrid systems by anchoring $ZnIn_2S_4$ on the Sb_2S_3 surface, which display significant enhancement of photocatalytic activity towards nitrogen photofixation under visible light irradiation. The optimized photocatalytic ammonia production activity of Sb_2S_3@$ZnIn_2S_4$ samples was successfully achieved by modulating the addition amount between Sb_2S_3 and $ZnIn_2S_4$. The photocatalytic experiment indicated that the optimal Sb_2S_3@$ZnIn_2S_4$-75 sample possessed the highest photocatalytic activity with an ammonia production rate of 15.96 ± 0.97 mg L^{-1} after visible light irradiation for 40 min, which was about 1.88 and 7.19 times higher than those of relevant $ZnIn_2S_4$ and Sb_2S_3, respectively. Such high efficiency in photocatalytic ammonia production was ascribed to faster charge separation originating from S-scheme charge separation. We hoped that our current investigation could provide some insights into the design and application of direct S-scheme hybrid systems for highly efficient photocatalytic activity towards nitrogen photofixation.

Data availability

The data supporting the findings of this study are available within the references, article and its ESI.†

Author contributions

C. J. Z. performed the experiments. C. Z. and H. X. Y. assisted with the N_2 photofixation experiments. T. C. and J. Z. carried out the characterization of materials. Z. H. and W. C. designed the research work. W. M. and G. L. carried out the theoretical calculations. W. C. wrote the manuscript. All authors discussed the results and commented on the manuscript.

Conflicts of interest

There are no conflicts to declare.

Acknowledgements

This work was supported by the National Natural Science Foundation of China (52102288), the Natural Science Foundation of Zhejiang Province (LTGS24E020001), the Project for Science and Technology Innovation Leading Talents of Zhejiang Provincial High-level Talents Special Support Plan (2021R52028), the National Training Program of Innovation and Entrepreneurship for Undergraduates, and the University Students' Scientific and Technological Innovation Activity Plan-Zhejiang Province New Talent Plan.

Notes and references

1 S. K. Boong, C. Chong, J. Zhang, T. R. Mogan, Y. Ni, H. Li and H. K. Lee, *Nano Energy*, 2024, **128**, 109922.
2 J. Wang, J. Gao, Y. Miao, D. Li, Y. Zhao and T. Zhang, *iScience*, 2024, **27**, 110088.
3 S. Z. Andersen, V. Čolić, S. Yang, J. A. Schwalbe, A. C. Nielander, J. M. McEnaney, K. Enemark-Rasmussen, J. G. Baker, A. R. Singh, B. A. Rohr, M. J. Statt, S. J. Blair, S. Mezzavilla, J. Kibsgaard, P. C. K. Vesborg, M. Cargnello, S. F. Bent, T. F. Jaramillo, I. E. L. Stephens, J. K. Nørskov and I. Chorkendorff, *Nature*, 2019, **570**, 504–508.
4 H. Li, J. Zhang, X. Deng, Y. Wang, G. Meng, R. Liu, J. Huang, M. Tu, C. Xu, Y. Peng, B. Wang and Y. Hou, *Angew. Chem., Int. Ed.*, 2024, **63**, e202316384.
5 T. Hu, G. Jiang, Y. Yan, S. Lan, J. Xie, Q. Zhang and Y. Li, *J. Mater. Sci. Technol.*, 2023, **167**, 248–257.
6 L. Wang, F. Guo, S. Ren, R.-T. Gao and L. Wu, *Angew. Chem., Int. Ed.*, 2024, **63**, e202411305.
7 N. Som, J. Y. Do and M. Kang, *Ceram. Int.*, 2017, **43**, 11250–11259.
8 F. Wang, C.-L. Yang, M.-S. Wang and X. Ma, *J. Power Sources*, 2022, **532**, 231352.
9 L. Li, X. Li, C. Yu and H. Li, *J. Alloys Compd.*, 2024, **1005**, 175999.
10 L. Xia, J. Zhang, Y. Peng, J. Yang, K. Hou, B. Xu, S. Li, B. Yang, W. Ma and X. Kong, *J. Mater. Sci.*, 2024, **59**, 14272–14283.
11 Z.-y. Zhu, J.-y. Li, W. Li, X.-y. Liu, Y.-y. Dang, T.-h. Ma and C.-y. Wang, *Environ. Sci.: Nano*, 2022, **9**, 1738–1747.
12 Q. Xu, C. Zheng, Z. Wang, Z. Zhang, X. Su, B. Sun, G. Nie and W. Yue, *J. Mater. Sci.*, 2022, **57**, 7531–7546.
13 L. Dashairya, S. Sharma, A. Rathi, P. Saha and S. Basu, *Mater. Chem. Phys.*, 2021, **273**, 125120.
14 W. Li, J. Li, T. Ma, G. Liao, F. Gao, W. Duan, K. Luo and C. Wang, *Small*, 2023, **19**, 2302737.
15 B. Garg, P. Hait and S. Basu, *J. Environ. Manage.*, 2024, **370**, 122403.
16 Y. Zhang, M. Gao, S. Chen, H. Wang and P. Huo, *Acta Phys.-Chim. Sin.*, 2023, **39**, 2211051.
17 Y. Wu, Y. Yang, M. Gu, C. Bie, H. Tan, B. Cheng and J. Xu, *Chin. J. Catal.*, 2023, **53**, 123–133.
18 X. Wu, G. Chen, L. Li, J. Wang and G. Wang, *J. Mater. Sci. Technol.*, 2023, **167**, 184–204.
19 L. Xiao, W. Ren, S. Shen, M. Chen, R. Liao, Y. Zhou and X. Li, *Acta Phys.-Chim. Sin.*, 2024, **40**, 2308036.
20 J. Luo, Z. Shi, J. Meng, F. Li, T. Li, M. Zhang, R. Greco and W. Cao, *J. Ind. Eng. Chem.*, 2023, **124**, 250–262.
21 Y. Xiao, H. Wang, Y. Jiang, W. Zhang, J. Zhang, X. Wu, Z. Liu and W. Deng, *J. Colloid Interface Sci.*, 2022, **623**, 109–123.
22 W. Li, J.-J. Li, Z.-F. Liu, H.-Y. Ma, P.-F. Fang, R. Xiong and J.-H. Wei, *Rare Met.*, 2024, **43**, 533–542.

23 J. Zhang, Z.-H. Pan, Y. Yang, P.-F. Wang, C.-Y. Pei, W. Chen and G.-B. Huang, *Chin. J. Catal.*, 2022, **43**, 265–275.
24 S.-Z. Lin, Y.-J. Yang, S.-Y. Jia, Z. Song, F. Feng, W. Chen, H. Yin and G.-B. Huang, *J. Alloys Compd.*, 2025, **1010**, 177619.
25 J. Zhang, X. Yang, C. Chen, Y. Li, J. Li, W. Chen, Y. Cui, X. Li and X. Zhu, *Chem. Mater.*, 2024, **36**, 12006–12017.
26 D. Zhang, D. Zhang, F. Zhao, Y. Zhao, H. Li, J. Liu, X.-Y. Ji, X. Pu and H. Zhang, *J. Mater. Chem. A*, 2024, **12**, 33546–33558.
27 Y.-Y. Ye, H.-Q. Yang, Z.-Y. Chen, W. Chen, J. Zhang, M. Zhang, L. Wang, Z. Song and G.-B. Huang, *J. Alloys Compd.*, 2025, **1010**, 178249.
28 G. John, H. Mohan, M. Navaneethan, S. Y. Ryu, B.-T. Oh and P. J. Jesuraj, *Chem. Eng. J.*, 2024, **500**, 157067.
29 G. Zhou, Y. Qi, Y. Wu, H. Wang, Z. Yan and Y. Wu, *J. Mater. Chem. A*, 2024, **12**, 28414–28423.
30 X. Li, K. Yang, F. Wang, K. Shi, W. Huang, K. Lu, C. Yu, X. Liu and M. Zhou, *J. Alloys Compd.*, 2023, **953**, 170064.
31 Z. Ma, Y. Yang, X. Wei, Q. Li, D. Zhang, Y. Wang, E. Liu and H. Miao, *ACS Appl. Nano Mater.*, 2024, **7**, 24213–24223.
32 X. Sun, X. Luo, X. Zhang, J. Xie, S. Jin, H. Wang, X. Zheng, X. Wu and Y. Xie, *J. Am. Chem. Soc.*, 2019, **141**, 3797–3801.
33 W. Yang, L. Xiao, W. Dai, S. Mou and F. Dong, *Adv. Energy Mater.*, 2024, **14**, 2303806.
34 W. Zhang, Q. Tan, T. Liu, Z. Liang, Y. Huang, Y. He, D. Han, D. Qin and L. Niu, *ACS Mater. Lett.*, 2024, **6**, 3007–3015.
35 M. Xia, B. Chong, X. Gong, H. Xiao, H. Li, H. Ou, B. Zhang and G. Yang, *ACS Catal.*, 2023, **13**, 12350–12362.
36 H. Feng, Q. Xu, T. Lv and H. Liu, *Appl. Catal., B*, 2024, **351**, 123949.
37 D. Cui, X. Yang, T. Zhang, M. Li and F. Li, *ACS Appl. Mater. Interfaces*, 2024, **16**, 30040–30054.
38 H. Liu, F. Zhang, H. Wang, J. Xue, Y. Guo, Q. Qian and G. Zhang, *Energy Environ. Sci.*, 2021, **14**, 5339–5346.
39 H. Liu, Y. Chen, H. Li, G. Wan, Y. Feng, W. Wang, C. Xiao, G. Zhang and Y. Xie, *Angew. Chem., Int. Ed.*, 2023, **62**, e202304562.
40 R. Lin, J. Wan, Y. Xiong, K. Wu, W.-c. Cheong, G. Zhou, D. Wang, Q. Peng, C. Chen and Y. Li, *J. Am. Chem. Soc.*, 2018, **140**, 9078–9082.
41 H. Zhao, D. Wang, X. Xue, X. Zhu, D. Ye, Y. Yang, H. Wang, R. Chen and Q. Liao, *J. Mater. Chem. A*, 2024, **12**, 15693–15704.
42 D. Zhou, S. Shao, X. Zhang, T. Di, J. Zhang, T. Wang and C. Wang, *J. Mater. Chem. A*, 2023, **11**, 401–407.
43 M. Zhang, M. Du, Y. Ren, Y. Zhu, Y. Dong, J. Liao, X. Chen, Q. Zheng and H. Yin, *J. Environ. Chem. Eng.*, 2024, **12**, 113261.
44 R. Li, K. Ba, D. Zhang, Y. Shi, C. Li, Y. Yu and M. Yang, *Small*, 2024, **20**, 2308568.
45 H. Yin, H. Chen, X. Feng, X. Chen, Q. Fei, Y. Zhang, Q. Zhao and Y. Zhang, *Int. J. Hydrogen Energy*, 2024, **51**, 433–442.
46 J. Cai, B. Liu, S. Zhang, L. Wang, Z. Wu, J. Zhang and B. Cheng, *J. Mater. Sci. Technol.*, 2024, **197**, 183–193.
47 E.-Z. Deng, Y.-Z. Fan, H.-P. Wang, Y. Li, C. Peng and J. Liu, *Inorg. Chem.*, 2024, **63**, 1449–1461.
48 W. Chen, W.-J. Zhang, K. Wang, L. Chang, R.-Q. Yan, X. Xiong, G.-B. Huang and D.-M. Han, *Langmuir*, 2023, **39**, 17830–17843.
49 M. Zhang, Y. Guan, Y. Dong, J. Liao, X. Chen and H. Yin, *J. Alloys Compd.*, 2023, **968**, 171947.
50 P. Liu, P. Chen, Z. Xing, Z. Li, H. Liu, Y. Wang, Y. Yang, Y. Wang and W. Zhou, *J. Mater. Chem. A*, 2024, **12**, 12155–12162.
51 J. Zhang, X. Jiang, J. Huang, W. Liu and Z. Zhang, *J. Mater. Chem. A*, 2022, **10**, 20048–20058.
52 Q. Yuan, J. Huang, A. Li, N. Lu, W. Lu, Y. Zhu and Z. Zhu, *Adv. Mater.*, 2024, **36**, 2311764.
53 Z. Zhang, J. Huang, Y. Fang, M. Zhang, K. Liu and B. Dong, *Adv. Mater.*, 2017, **29**, 1606688.
54 M. Zhou, Z. Guo, Q. Song, X. Li and Z. Liu, *Chem. Eng. J.*, 2019, **370**, 218–227.
55 W. Guan, L. Zhang, P. Wang, Y. Wang, H. Wang, X. Dong, L. Yu, Z. Gan, L. Dong and L. Sui, *J. Mater. Chem. A*, 2024, **12**, 12181–12189.